Two-dimensional Photocatalysts Design: A Critical Review of Recent Experimental and Computational Advances

Yunxuan Zhao, Shuai Zhang, Run Shi, Geoffrey I.N. Waterhouse, Junwang Tang and Tierui Zhang*

((Optional Dedication))

Y. Zhao, S. Zhang, Dr. R. Shi, Prof. T. Zhang

Key Laboratory of Photochemical Conversion and Optoelectronic Materials, Technical Institute of Physics and Chemistry, Chinese Academy of Sciences, Beijing 100190, China

Fax: +86 10 62554670 Tel: +86 10 82543428

E-mail: tierui@mail.ipc.ac.cn

Y. Zhao, S. Zhang, Prof. T. Zhang

Center of Materials Science and Optoelectronics Engineering, University of Chinese Academy of Sciences, Beijing 100049, China

Prof. G. I.N. Waterhouse

School of Chemical Sciences, The University of Auckland, Auckland 1142, New Zealand

Prof. J. Tang

Dept of Chemical Engineering, University College London, London WC1E 7JE, UK

Abstract

In recent years, two-dimensional (2D) semiconductor photocatalysts have been widely applied in water splitting, CO_2 reduction, N_2 fixation, as well as many other important photochemical reactions. Photocatalysts in the form of 2D nanosheet possess many inherent advantages over traditional 3D nanopowder photocatalysts, including improved light absorption characteristics, short electron and hole migration paths to the photocatalysts' surface (thus minimizing undesirable electron-hole bulk

recombination), and abundant surface defects which allow band gap modulation and facilitate charge transfer from the semiconductor to adsorbates. When synergistically exploited and optimized, these advantages can impart 2D photocatalysts with remarkable activities relative to their 3D counterparts. Accordingly, a wide range of experimental approaches is now being explored for the synthesis of 2D photocatalysts, with computational methods increasingly being used for prediction of promising new 2D photocatalytic materials. Herein, we critically review recent literatures related to 2D photocatalysts development and design. Particular emphasis is placed on 2D photocatalysts synthesis and the importance of computational studies on the fundamental understanding of 2D photocatalyst electronic structure, band gap structure, charge carrier mobility and reaction pathways. We also overview the practical challenges of using 2D photocatalysts, such as their difficulty to synthesize in large quantity and also their characterization. The overarching aim of this review is to provide a snapshot of recent work targeting high-performance 2D photocatalysts for efficient solar energy conversion, thus forming a firm base for future advancements in this rapidly expanding area of photocatalysis research.

1. Introduction

Global warming caused by the combustion of fossil fuels for electricity generation and transportation has catastrophic environmental consequences [1], motivating the search for alternative renewable energy technologies that are clean (i.e. sustainable with a near-zero carbon footprint) and economically viable, thus enabling a progressive transition away from fossil fuel energy in the near future [2]. Solar energy capture and utilization through semiconductor photocatalysis represent a very promising future technology for the production of fuels, including H_2 *via* water splitting or biomass photoreforming, hydrocarbon fuels via CO_2 reduction, and ammonia synthesis by photocatalytic N_2 fixation [3-6]. These approaches rely on the ability of certain semiconductor materials to be photoexcited under sunlight to create charge carriers (conduction band electrons and valence band holes) with appropriate energies needed to drive specific photocatalytic reactions on the semiconductor surface. To achieve reasonable reaction rates under direct solar illumination, semiconductor photocatalysts of nanoscale dimensions are used, thereby maximizing the generation and availability of charge carriers whilst also ensuring an abundance of surface sites for hole-mediated oxidation or electron-mediated reduction reactions [7-9]. In recent years, as a means of further enhancing the rates of photocatalytic reactions, researchers have focused their attention on low-dimensional semiconductor photocatalysts (e.g. 1D nanowires or 2D nanosheets), with these anisotropic-shaped photocatalysts demonstrating remarkable performance in a wide range of different photocatalytic reactions. Morphology control during photocatalyst synthesis is essential to exploiting the inherent photophysical advantages offered by 1D and 2D photocatalysts, necessitating the development of new synthetic approaches towards such novel low-dimensional semiconductor materials.

Following the discovery that 2D graphene possessed outstanding physical and electronic properties [10-12], numerous other 2D nanosheet materials have been systematically investigated, including layered transition metal dichalcogenides (TMDs) [13], metal oxides [14, 15], layered double hydroxides (LDHs) [16], hexagonal boron nitride (h-BN) [17], graphitic carbon nitride (g-C_3N_4) [18], MXenes [19], and black phosphorus [20], amongst others. These 2D nanomaterials have found various

applications dictated by their intrinsic physical and chemical properties [21], with a number of the aforementioned materials being semiconducting, thus attracting interest for photocatalytic applications. The benefits of a 2D structure for photocatalysis relates to four main aspects: (1) a large photocatalyst specific surface area, thus offering an abundance of highly-exposed active sites; (2) short transport paths for photoexcited holes and electrons to the photocatalyst surface for reaction, thus minimizing bulk electron-hole pair recombination with limits the efficiency of traditional 3D photocatalysts; (3) improved conductivity (due to abundant surface defects) which benefits charge transfer to adsorbates; and (4) improved mechanical properties (excellent durability), typically when 2D photocatalysts are composited with other materials [22]. Whilst considerable fundamental advancements have been made over the past few years regarding the synthesis of 2D photocatalytic nanomaterials, reactions rates for processes such as water splitting and CO_2 reduction remain too low to warrant serious consideration as a practical technology towards solar fuels. The discovery of more efficient 2D photocatalysts (with reaction rates at least 100 times higher than current state-of-the-art systems) is an urgent priority for technology transfer to industry.

The traditional approach used to synthesize catalysts and photocatalysts is highly iterative, wherein a broad range of materials are synthesized, after which the performance of all the materials is evaluated for a given reaction. The most active catalysts/photocatalysts identified through this screening process are then subjected to further investigation, typically involving their composition and structure being modified slightly and their performance again measured. By such a laborious approach, a catalyst or photocatalyst with good overall performance characteristics is eventually identified. In recent years, computational approaches have emerged as an alternative strategy for screening catalysts for particular reactions, with parameters such as high efficiency, high selectivity and cost guiding the selection of elements used to guide the catalyst discovery phase. Such computational screening of catalytic materials typically requires a supercomputer, an advanced simulation package and an experienced programmer. Density functional theory (DFT)-based first-principle calculations are also widely utilized to explore the properties of materials, as well as the role of different

components in the catalytic mechanism or overall reaction cycle [23]. Further, theoretical simulation provides a framework for understanding catalysis on both mesoscopic and microscopic levels (molecular, atom or electron). In 2011, Ye's group reviewed photocatalysis processes (e.g. photoexcitation, transfer of carriers and catalytic reactions) that had been studied theoretically using electronic structure calculations and molecular dynamics simulations [1]. Similarly, Yang *et al.* explored the significance of theoretical simulation in photocatalyst design for photocatalytic water splitting [23]. These computational works serve to useful guide for experimentalists in the rational design of new or improved 2D photocatalysts with superior photocatalytic performance.
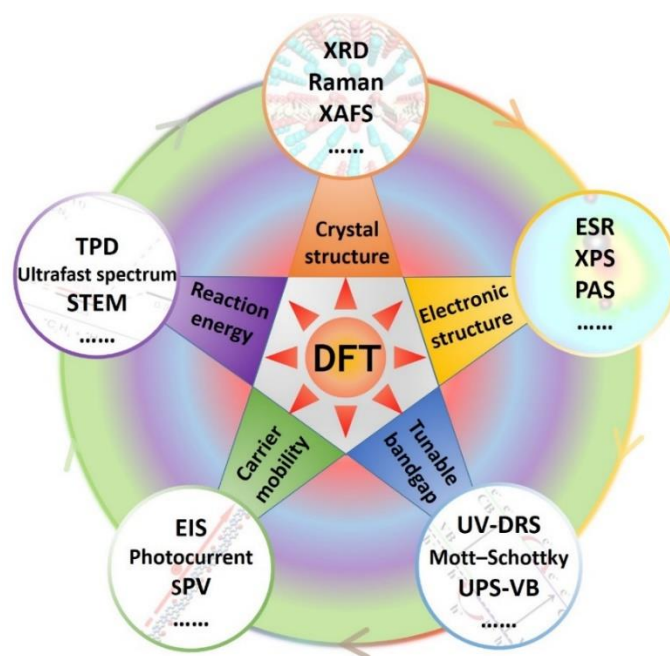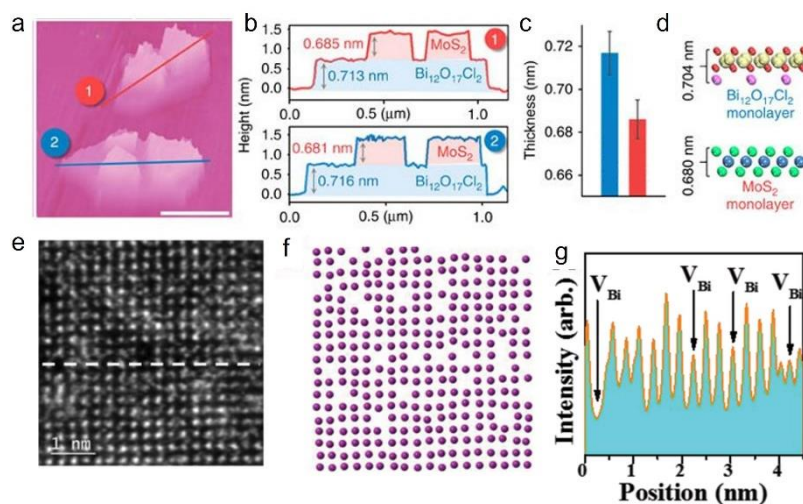

FIGURE 1

Design and development of 2D photocatalytic systems by combining advanced characterization methods with computational simulations based on density functional theory (DFT)-based first-principle calculations (XRD: X-ray diffraction; XAFS: X-ray absorption fine structure; ESR: electron spin resonance; XPS: X-ray photoelectron spectroscopy; PAS: Positron annihilation spectroscopy; UV-DRS: UV–vis diffuse reflectance spectra; UPS-VB: ultraviolet photoelectron spectroscopy-Valence band; EIS: electrochemical impedance spectroscopy; SPV: surface photovoltage method; TPD: temperature programmed desorption

and STEM: scanning transmission electron microscopy).

In this review, we provide an overview of recent advances in 2D photocatalyst development/design encompassing experimental studies and simulation. Specific foci include 2D photocatalyst: i) crystal structure, ii) electronic structure, iii) bandgap energies, iv) carrier mobility and v) reaction energy pathways, together with the optimization of these for efficient performance. In addition, technical challenges to the development and application of 2D photocatalysts are also discussed. The usefulness of computational methods for 2D photocatalyst screening/development/design is strongly emphasized, guiding researchers in the appropriate choice of materials and experimental methodologies for 2D photocatalyst synthesis, as well as the type of techniques needed for photocatalyst characterization (Fig. 1). Smart application of computational and experimental approaches is essential for the rational design of 2D photocatalysts and step-change improvements in performance (i.e. to move the field beyond serendipitous discovery followed by subsequent research towards catalyst optimization).

FIGURE 2

a) Side-view 3D AFM images and b) corresponding height profiles along the red and blue lines in a. c-d) The average measured thicknesses and the theoretical thicknesses, respectively, of mono-layered $Bi_{12}O_{17}Cl_2$ and MoS_2 in 2D Janus materials [24]. Copyright 2016, Nature Publishing Group. e) atomic-

resolution STEM-HAADF images of defect-rich Bi_3O_4Br following Gaussian filtering to remove noise, f) structural model to show surface Bi defects in e; purple spheres indicate Bi atoms, whilst surface Bi vacancies are represented as blanks in the model, and g) line profile of defect-rich Bi_3O_4Br along the dotted line shown in d [25]. Copyright 2019, Wiley-VCH.
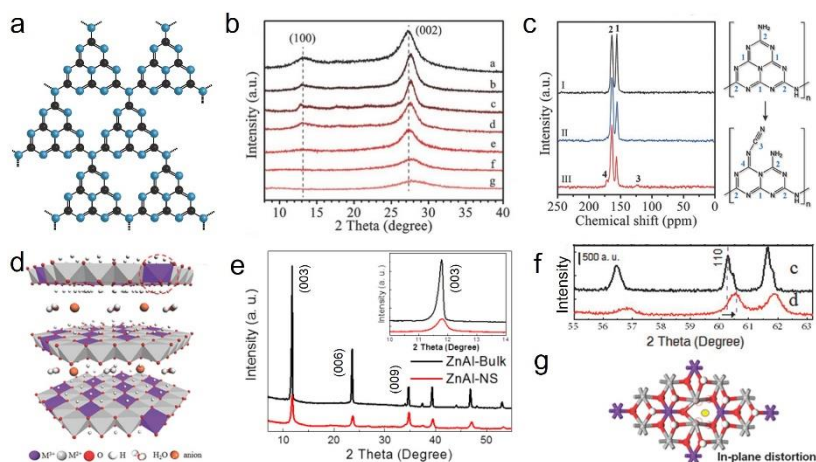
FIGURE 3

a) Schematic showing the structure of g-C_3N_4. b) XRD patterns for g-C_3N_x containing different amounts of –C≡N groups. a-g) represent pristine g-C_3N_4, g-C_3N_x-0.005, g-C_3N_x-0.01, g-C_3N_x-0.05, g-C_3N_x-0.1, g-C_3N_x-0.5, and g-C_3N_x-1.0, respectively. c) Solid-state ^{13}C MAS NMR spectra of (I) g-C_3N_4, (II) g-C_3N_x-0.05, and (III) g-C_3N_x-0.5, and the structures of the heptazine units before and after introducing cyano groups [35]. Copyright 2017, Wiley-VCH. d) Polyhedral representation of ultrathin LDH nanosheets with defective MO_6 octahedra at the nanosheet edges or on the surface. e-f) XRD patterns of bulk ZnAl-LDH and defect-rich ZnAl-LDH nanosheets. g) Top-view 2D structural model for an LDH monolayer from DFT calculations [40]. Copyright 2017, Wiley-VCH.

2. Combining Theory with Experiment

2.1 Crystal structure

The use of theoretical simulation in catalysis is a rapidly developing area of research. However, such approaches need to be implemented with a degree of caution,

since the working state and crystal structure of many catalysts under reaction conditions remain difficult to pinpoint. Thus, to ensure a good approximation to experiment and the real crystal structure, the supercell used in the simulations should be constructed based on detailed catalyst characterization studies. Advancements in catalyst characterization over the past decade, including both microscopy-based and spectroscopy-based techniques, now enable the composition and structure of catalysts to be accurately surveyed at the atomic scale. Notable recent advances in catalyst characterization include 3D topographic atomic force microscopy (AFM) and aberration-corrected high-angle annular dark-field scanning transmission electron microscopy (HAADF-STEM). Ultrathin 2D materials with atomic thickness expose an abundance of active sites that enhance their photocatalytic activity. AFM is the arguably the most effective method for the measurement of the thickness of 2D materials. Zhang *et al.* successfully synthesized 2D Janus (Cl_2)-($Bi_{12}O_{17}$)-(MoS_2) bilayer junctions [24], with the bilayer structure able to be directly probed by AFM analysis (Fig. 2a-c). Height profiles taken from the AFM images revealed layers of thickness 0.686 nm and 0.717 nm, corresponding closely with the theoretical thicknesses of the MoS_2 and $Bi_{12}O_{17}Cl_2$ monolayers, respectively (Fig. 2d). HAADF-STEM also allows the determination of 2D nanosheet thicknesses, offering the additional advantage of being able to directly observe the atomic structure. Typically, abundant point defects are present in ultrathin 2D nanosheets, which can be created during nanosheet synthesis or through post-synthetic modifications. As shown in Fig. 2e-g, the surface of defect-rich Bi_3O_4Br is missing a number of Bi and O atoms, with such vacancies introducing lattice disorder and offering a wealth of unsaturated coordination sites for reactant adsorption. Such lattice disorder and vacancies can be highly beneficial for photocatalytic reactions [25]. X-ray diffraction (XRD) is a widely applied technique for examining the structure of 2D materials, which can have quite distinct and characteristic diffraction patterns due to their nanosheet habit and distorted unit cells [16, 26]. Graphitic carbon nitride (g-C_3N_4), a polymeric compound composed of heptazine units (Fig. 3a), has recently received a lot of attention owing to its excellent photocatalytic activity under visible light ($\lambda > 420$ nm). The XRD pattern of g-C_3N_4 contains two characteristic peaks which

arise from diffraction on (100) and (002) crystal planes (Fig. 3b) [27-31], corresponding to in-plane packing and interplanar stacking of g-C$_3$N$_4$ nanosheets, respectively. The position and intensity of these reflections depend on the functional groups present in g-C$_3$N$_4$, as evidenced by the change in XRD patterns seen in Fig. 4b as –C≡N groups would be progressively introduced. Solid-state ^{13}C magic angle spinning (MAS) NMR measurements provided further evidence for the successful introduction of cyano groups (Fig. 3c) [32]. The NMR spectrum of pristine g-C$_3$N$_4$ shows two strong peaks at 156.4 and 164.5 ppm, which can be assigned to C$_{3N}$ (1) and C$_{2N-NHx}$ (2) moieties in the heptazine units [33]. As cyano groups were introduced, two new peaks located at 123.8 and 171.0 ppm appeared corresponding to the cyano carbon atom (3) and the neighbor C atom (4), respectively [34,35]. Similar to g-C$_3$N$_4$, layered-double-hydroxide (LDH) nanosheet photocatalysts also have characteristic XRD patterns, exemplified by interplanar (00l) reflections and in-plane (110) peaks (Fig. 3d-e). By analysis of the (00l) family of planes based, the lattice parameter c can be calculated as $c = 3\ d(003)$, allowing the type of intercalated anion can be determined [36-38]. Together with the lattice parameter a, calculated as $a = 2\ d(110)$, the unit cell size for the LDH nanosheets can be estimated [39]. In Fig. 3f, the (110) reflection for zinc-aluminium LDH nanosheets (ZnAl-NS) was observed at higher 2θ angles than that measured for the bulk lamella LDH material (ZnAl-Bulk), which was ascribed to compressive (negative) strain in the ab-plane of ZnAl-NS (Fig. 3g) [40]. Raman spectroscopy is another technique that can provide useful structural information about 2D photocatalyst [26, 41]. BiOCl shows four Raman bands at 61, 143, 202, and 400 cm^{-1} (Fig. 4a) [42, 43]. Oxygen vacancies (Vo) give rise to an additional peak at 98 cm^{-1} [44]. After treatment with H$_2$O$_2$, the peak at 98 cm^{-1} associated with Vo in Fig. 4a disappeared, demonstrating that H$_2$O$_2$ absorbed at Vo sites where it was reduced by H$_2$O$_2$. After the infrared irradiation, the Vo peak at 98 cm^{-1} reappeared, though with lower intensity compared to pristine BiOCl. Results indicate that the amount of Vo sites was lowered following treatment with H$_2$O$_2$ treatment and infrared irradiation. X-ray absorption fine structure (XAFS) as a very powerful technique for exploring the local atomic structure of metals in 2D photocatalysts, and was successfully applied to the study of BiOCl nanosheets

[42, 45]. Bi L$_3$-edge EXAFS R space spectra for BiOCl nanosheets containing different amounts of Vo (OV-3 = high concentration of Vo, OV-0 = no Vo) are shown in Fig. 4b. The spectra show peaks at 1.8 Å and 3.7 Å, corresponding to the first Bi-O shell and Bi-Bi shell, respectively. The intensity of the Bi-O shell feature increased as the Vo concentration in the BiOCl nanosheets decreased (Fig. 4c), reflecting the increased Bi-O coordination number and less severe structural distortions caused by the elimination of oxygen vacancies with H$_2$O$_2$ and infrared treatments (as depicted in Fig. 4c). The EXAFS data thus complements the findings of the in-situ Raman investigation.
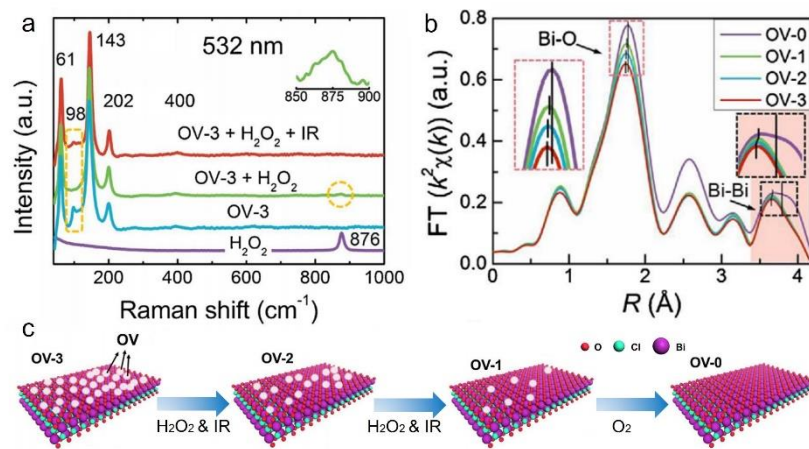
FIGURE 4

a-b) In-situ Raman spectra and Fourier-transform Bi L$_3$-edge EXAFS spectra for BiOCl samples treated with H$_2$O$_2$ and infrared irradiation. c) The schematic diagram of BiOCl samples with different concentration of Vo [42].Copyright 2018, Elsevier.
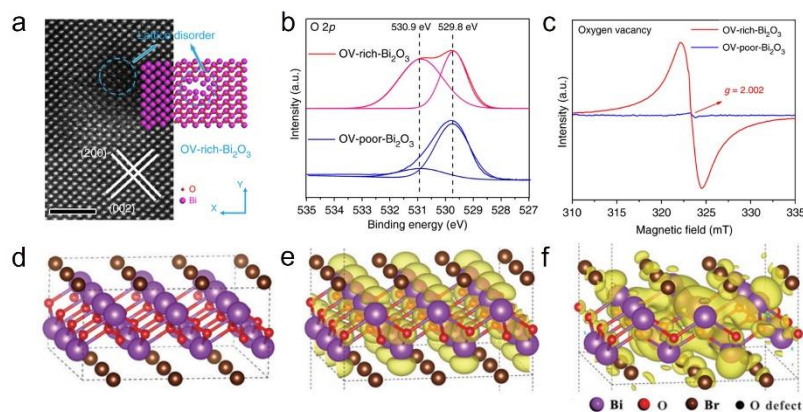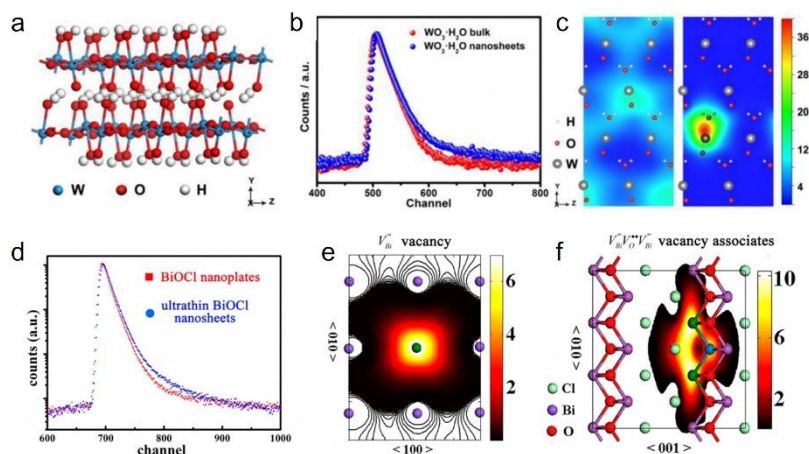
FIGURE 5

a) Atomic-resolution HAADF-STEM images and corresponding structure model of oxygen deficient Bi_2O_3 nanosheets. The scale bar is 2 nm. b-c) O 2p XPS spectra and room-temperature ESR spectra of Bi_2O_3 nanosheets rich and poor in Vo, respectively [48]. Copyright 2019, Nature Publishing Group. d-f) Calculated charge density contour plots at the conduction band edge for bulk BiOBr, ultrathin BiOBr nanosheets, and oxygen deficient ultrathin BiOBr nanosheets [51].Copyright 2018, Wiley-VCH.

2.2 Electronic structure

Considering that photocatalytic reactions occur on the surfaces of photocatalysts, the electronic structure of exposed surface facets strongly influences photocatalytic performance [46, 47]. Accordingly, the modification of the electronic structure of photocatalysts has been widely pursued with a view to achieving the improved activity. Many strategies have been applied to tune electron densities on the surface of the photocatalysts. For example, Chen and co-workers introduced Vo in Bi_2O_3 atomic layers [48], leading to differences in charge density and electron-rich regions neighboring the Vo (Fig. 5a). X-ray photoelectron spectroscopy (XPS) was used to follow the changes in the electronic structure of Bi_2O_3 with the introduction of Vo. The O 2p XPS spectrum of pristine Bi_2O_3 showed an intense lattice oxygen peak at 529.8 eV. On introduction of Vo, an additional feature appeared at 530.9 eV associated with coordinatively unsaturated oxygen anions (Fig. 5b) [49, 50]. Electron spin resonance (ESR) for the Vo-rich Bi_2O_3 nanosheets showed an ESR signal with g = 2.002, which could readily be assigned to electrons trapped by Vo (Fig. 5c). Conversely, the Vo-poor sample was almost ESR inactive [43, 50]. DFT calculations shed further light on the role of Vo in trapping photoexcited electrons in nanosheet photocatalysts. For BiOBr nanosheets with rich Vo, the charge distribution was found to be more delocalized in the vicinity of Vo (Fig. 5d-f), which was rationalized by the overlap of the electronic orbitals on Bi atoms in defect-rich BiOBr [51, 52]. The delocalized electrons around surface Vo sites served to promote the reduction of surface adsorbates, thus enhancing

photocatalytic performance.

FIGURE 6

a) Crystal structure of orthorhombic $WO_3 \cdot H_2O$ b) Positron lifetime spectrum of ultrathin and bulk $WO_3 \cdot H_2O$. c) Schematic representations of trapped positrons on $V''''_{[OWOH2]}$ vacancies [55]. Copyright 2015, American Chemical Society. d) Positron lifetime spectrum of ultrathin BiOCl nanosheets and BiOCl nanoplates. e-f) Schematic of trapped positrons for a V''''_{Bi} defect and $V''''_{Bi}V_{\ddot{O}}V''''_{Bi}$ vacancy [56]. Copyright 2013, American Chemical Society.

Positron annihilation spectroscopy (PAS) as a well-established technique for determining the type and relative concentration (down to ppm levels) of various defects/vacancies in 2D photocatalysts [53, 54]. Fig. 6a shows the crystal structure of orthorhombic $WO_3 \cdot H_2O$ [55]. As the thickness of $WO_3 \cdot H_2O$ nanosheets was reduced from 50 nm to close to the atomic scale (2-3 nm), the electronic structure of the exposed facets changed, thus changing the lifetime of positrons in $WO_3 \cdot H_2O$. A longer positron lifetime for the ultrathin nanosheets is the presence of large voids, bulk defects and complex vacancies ($V''''_{[OWOH2]}$) (Fig. 6b-c). The same trend was seen in BiOCl materials [56]. As the thickness of BiOCl nanosheets was reduced, their positron lifetime increased (Fig. 6d). The extended lifetime was explained by the evolution of bismuth vacancies from isolated V''''_{Bi} defects to triple vacancies $V''''_{Bi}V_{\ddot{O}}V''''_{Bi}$ (Fig. 6e-f) with decreasing nanosheet thickness, with the triple vacancies causing more efficient separation of photo-generated electron-hole pairs and improved photocatalytic activity.

Simulations of the electronic structure of existing 2D materials enable the design of new and more efficient 2D materials with programmable electronic structures. Rigorous and detailed experimental studies provide a reliable basis set for such theoretical simulations.
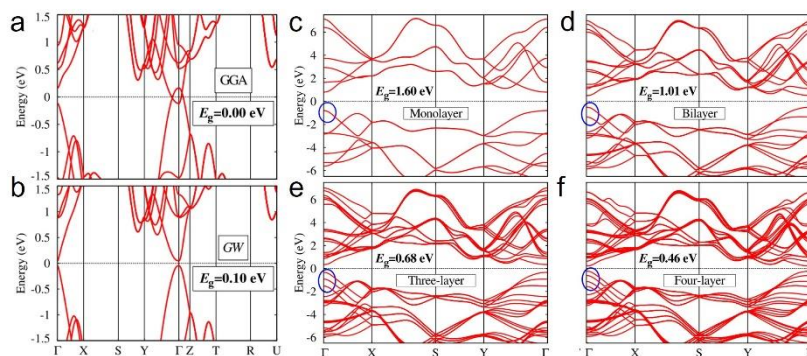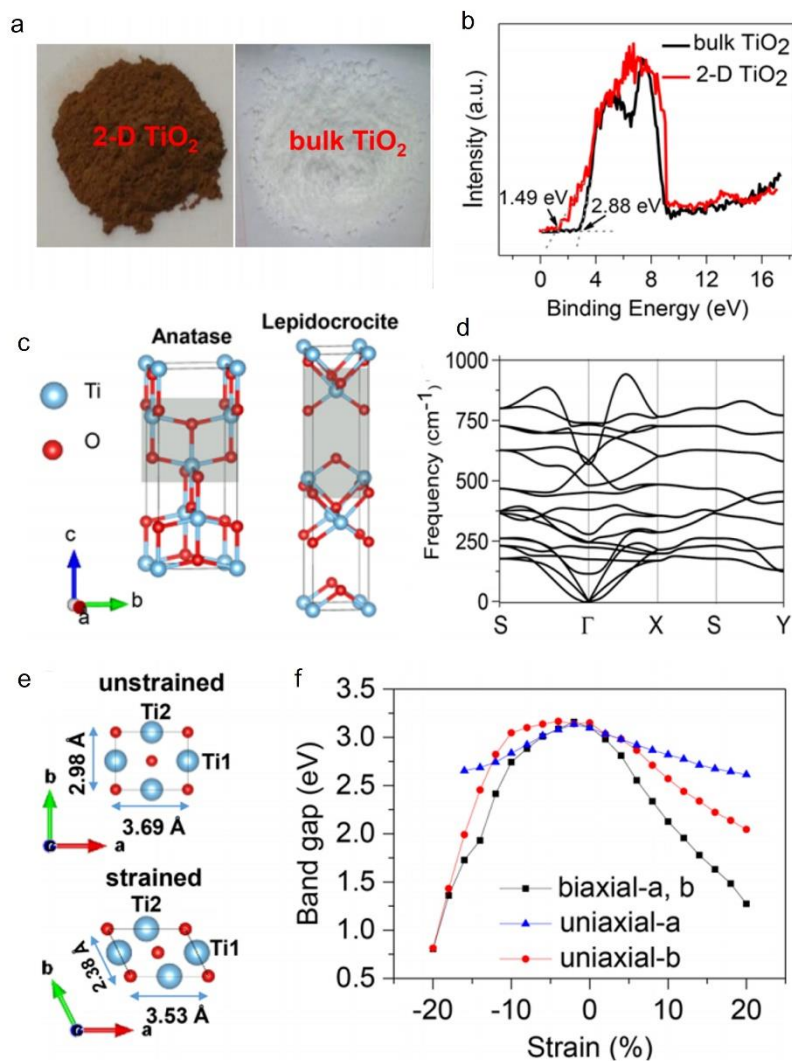

FIGURE 7

a-b) Band structures of bulk black phosphorus (BP) calculated by using density functional theory-General Gradient Approximation (DFT-GGA) and a more accurate one-body Green's function (GW) approach along the high-symmetry points of the Brillouin zone. c-f) Band structures BP with different thicknesses calculated using the GW approach. Reproduced with permission [62]. Copyright 2014, American Physical Society.

2.3 Band gap modulation

Light absorption leading to photo-excitation is a key step in any photocatalytic reaction [57, 58]. The "leaf-like" structure of 2D materials makes them near ideal light-harvesting architectures, with a narrow band gap also being important for effective solar spectrum utilization. For efficient photocatalysis, the valence and conduction band edge positions must be well-matched to the redox potential(s) of the reaction(s) of interest [59-61]. In order to achieve both efficient light absorption and appropriate band edge positions, band gap modulation is often necessary. To achieve this in a controlled manner, theoretical calculations are invaluable and advantageous. Taking black phosphorus (BP) as an example, it was found that the bandgap (and thus band edge locations) in this 2D layered material could be adjusted simply by varying the number

of the atomic layers in the material. Rudenko *et al.* applied General Gradient Approximation (GGA) and one-body Green's function (GW) approximation to calculate the band structure of monolayer and few-layer BP (Fig. 7a-b). An increase in the bandgap (E_g) was found as the number of BP layers was reduced from four to one (Fig. 7c-f). Experimental data for BP materials confirmed that varying the number of BP layers allows bandgap tuning [62]. Molybdenum disulfide (MoS_2) showed a similar change in bandgap structure as a function of thickness (i.e. the number of layers). The structure of a MoS_2 monolayer is comprised of two hexagonal planes of S atoms and an intermediate hexagonal plane of Mo atoms. Computational studies predicted that MoS_2 transforms from an indirect-gap semiconductor to a direct-gap semiconductor as the number of layers is reduced to near a monolayer. The direct excitonic transition energy (direct-gap) at the Brillouin zone K point is invariant to the number of layers, but the indirect bandgap (arrow) increases as the number of layers is reduced to only a few [63]. Optical measurements further supported the computational findings. Monolayer MoS_2 showed a single photoluminescence emission peak at 1.90 eV (corresponding to the direct-gap energy). As the number of MoS_2 layers increased, the photoluminescence emission maximum progressively redshifted to lower energies, eventually reaching 1.29 eV (the indirect-gap energy) [64].

FIGURE 8

a) Photographs of as-synthesized 2D TiO_2 (red powder) and bulk TiO_2 (white powder). b) UPS-VB spectra of 2D TiO_2 and bulk TiO_2 referenced to the Fermi level (E_F = 0 eV). c) Structures of bulk anatase and lepidocrocite TiO_2. d) Calculated phonon dispersion of a lepidocrocite TiO_2 monolayer. e) Top views of the structure of a lepidocrocite TiO_2 monolayer in the strained and unstrained states. f) Calculated band gap energy as a function of different uniaxial and biaxial strains for a lepidocrocite TiO_2 monolayer [70]. Copyright 2017, American Chemical Society.
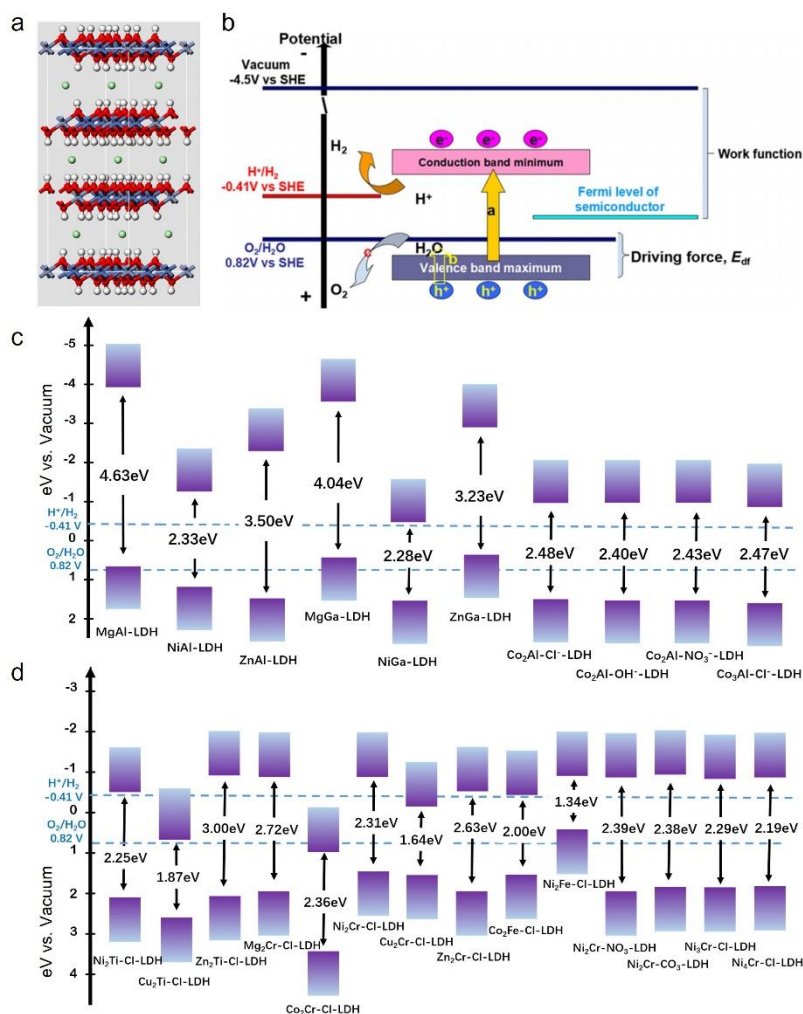
FIGURE 9

a) Optimized geometry of a layered double hydroxide (LDH). b) Schematic diagram of photocatalytic water splitting to produce H_2 and O_2 at pH 7. The driving force (E_{df}) and work function (*W*) are indicated. c) Calculated band gap energies and band edge positions for 24 different LDH materials [73]. Copyright 2017, American Chemical Society.

Transition metal oxides represent the most widely studied class of photocatalytic materials. Accordingly, oxides nanosheets have been the subject of intensive investigation. Amongst these, titanium oxide nanosheets and niobium oxide nanosheets have received the most attention [65-68]. $Nb_3O_8^-$ and $Ca_2Nb_3O_{10}^-$ possess a perovskite-like layered structure in which NbO_6 octahedra are linked *via* corner-sharing, while

$TiNbO_5^-$, $Ti_2NbO_7^-$, and $Ti_5NbO_{14}^{3-}$ are constructed from Ti/NbO_6 octahedra *via* edge and corner-sharing. Sasaki *et al.* found that the bandgap energies of the 2D versions of these indirect wide-gap metal oxides were significantly larger than in the bulk counterparts due to quantum confinement effects [65]. Similarly, the bandgap of single-layered TiO_2 is larger than that of bulk rutile TiO_2 or bulk anatase TiO_2, with close agreement found between the band edge positions determined from theoretical simulations and photoelectrochemical tests [69]. However, for 2D materials, intrinsic strain and lattice distortions can substantially alter the energy band structure. Xu *et al.* reported the synthesis of free-standing 2D TiO_2 with a crumpled morphology through a one-step solvothermal method [70]. The 2D structure resembled (Fig. 8a-c) the lepidocrocite TiO_2 phase which exists stably in monolayer form. The 2D structure was verified by the absence of any imaginary phonon frequencies (Fig. 8d). This 2D TiO_2 material possessed a very narrow optical band gap ($\sim$1.84 eV) and red color, thus being quite distinct from bulk TiO_2 (white, Eg $\sim$3.1-3.3 eV). VB photoemission spectra determined that the VB level (comprising mainly O 2p states) was shifted significantly upwards in the 2D TiO_2 relative to bulk TiO_2, thus narrowing the band gap. Using the atomic structure models shown in Fig. 8e, DFT calculations were performed within the local density approximation (LDA) to investigate the effect of lattice strain on the bandgap energy of 2D TiO_2. The calculations demonstrate that the band gap in 2D TiO_2 could be tuned from 3.1 eV to 0.8 eV depending on the degree of compressive strain in the 2D material (Fig. 8f).

Layered double hydroxide (LDH) nanosheets and bismuth oxyhalides (BiOX, X= F, Cl, Br, I) nanosheets have recently emerged as promising 2D photocatalytic materials [16, 71]. They share many attractive properties, such as tunable composition and morphology, whilst allowing photocatalysts with ideal band edge positions to be synthesized for a particular reaction. LDH materials have the general molecular formula $[M^{2+}_{1-x}M^{3+}_x(OH)_2]^{q+}(A^{n-})_{q/n}\cdot yH_2O$, containing divalent and trivalent metal cations and charge stabilizing anions (A^{n-}). The M^{2+} and M^{3+} cations are octahedrally coordinated by oxygen atoms in LDH sheets, whilst the anions and water occupy the interlayer galleries (Fig. 9a). Simply by varying the metals in the LDH material, the bandgap

energy and band edge positions can be easily adjusted. Theoretical calculations [72, 73] allow the band edge positions and bandgap energies for LDHs with different unit cell structures to be predicted with high precision (Fig. 9b-d), thereby guiding experimentalists in the correct selection of cations, M^{2+}/M^{3+} cations ratio and anions to realize a photocatalyst with specific optical properties for a given photocatalytic reaction. Similarly, BiOX is composed of [-O-Bi-] layers with interlayer halogen ions (X^-) [71, 74]. The BiOX band structure can be modified simply by altering the type of interlayer halogen ions. Deformation density (DD) calculations were used to examine the electron density interactions between O and Bi and also X and Bi in BiOX, with X identified as playing a key role in the developed band structures and electron-transfer processes during photocatalysis. For Eu-doped BiOX, the CB minimum (CBM) was invariant to X, whereas the VB maximum (VBM) shifted up considerably with an increase in the atomic number of X. This is explained by the large contribution of X-np states to the VBM, whereas the CBM comprises Bi 6p antibonding states and thus is not be impacted greatly by the X anion [75]. The isolated Eu^{3+} dopant imparted Eu-doped BiOX with excellent photoluminescence and photocatalytic properties. Furthermore, the introduction of N defects was shown to narrow the bandgap of 2D g-C_3N_4 whilst also promoting electron transfer, thereby enhancing the photocatalytic activity [35]. As the concentration of N-defects increased, the CBM of g-C_3N_4 shifted downward causing band gap narrowing, resulting in enhanced light absorption. DFT calculations of the band structure and partial density of states revealed the appearance of defect states in band gap of N defect-rich g-C_3N_4, hence the increased visible light response.
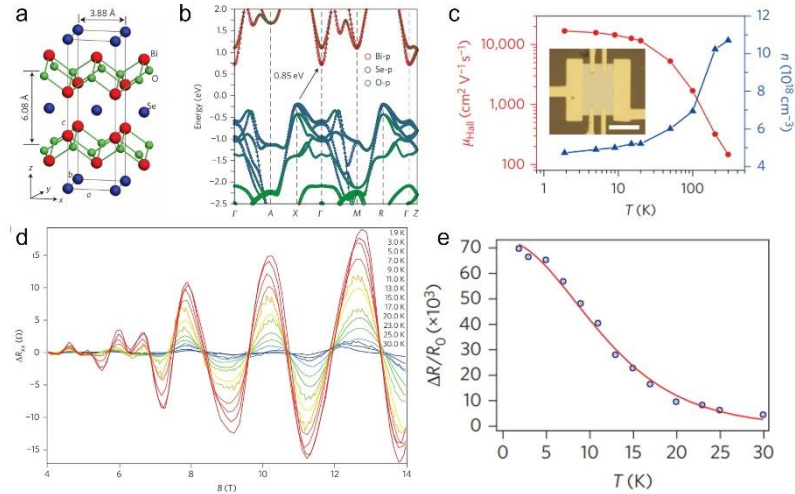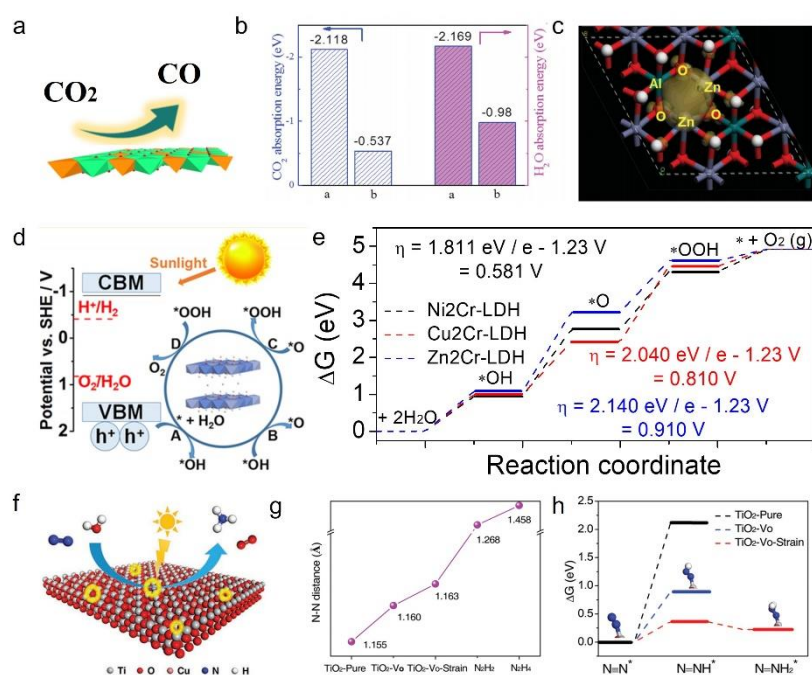
FIGURE 10

a) Layered crystal structure of Bi_2O_2Se. b) Calculated band structure of Bi_2O_2Se showing a bandgap of ~0.85 eV. c) Hall mobility (μHall) and carrier density (n) as a function of temperature in a Bi_2O_2Se nanoplatelet. Inset: optical microscopy image of a Hall-bar device fabricated on the Bi_2O_2Se nanoplatelet with a thickness of ~20.9 nm. Scale bar, 20 μm. d) SdH oscillatory part of the longitudinal magnetoresistance ΔR_{xx} as a function of applied perpendicular magnetic field measured in the temperature range from 1.9 to 30 K. The non-oscillatory part was removed by subtracting a high-tolerance smoothing spline fit. e) Temperature-dependent $\Delta R/R_0$ values of the SdH oscillations and the Lifshitz–Kosevich fitting at 12.8 T, giving a low cyclotron in-plane effective mass of 0.14 ± 0.02m_0 [80]. Copyright 2017, Nature Publishing Group.

2.4 Carrier mobility

Whilst significant fundamental advancements have been made in recent years relating to the application of 2D materials in photocatalysis, solar-to-chemical conversion efficiencies remain far too low to justify serious practical interest. Low carrier mobilities are one of the main limiting factors [76-79]. For example, the carrier mobility of layered transition metal dichalcogenides (TMDs) is typically below 300 cm^2 V^{-1} S^{-1}. The discovery and design of 2D semiconductor photocatalysts with higher carrier mobilities are imperative. Recently, Peng's group successfully prepared layered tetragonal Bi_2O_2Se through chemical vapor deposition, consisting of planar covalently bonded oxide layers (Bi_2O_2) sandwiched by Se square arrays (Fig. 10a) [80]. The bandgap of Bi_2O_2Se was investigated *via* both DFT calculations and angle-resolved photoemission spectroscopy measurements. The results show that Bi_2O_2Se possesses

an indirect bandgap of 0.85 eV (Fig. 10b). The carrier mobility of high-quality Bi_2O_2Se nanoplatelets was measured directly using a standard Hall-bar device (processing without inert gas protection) [81, 82]. As shown in Fig. 10c, the Hall mobility of Bi_2O_2Se reached as high as 28900 cm^2 V^{-1} S^{-1} at 1.9 K. The long mean free path of the highly mobile electrons in Bi_2O_2Se enabled the observation of Shubnikov-de Haas (SdH) quantum oscillations (Fig. 10d). The normalized amplitudes at 12.8 T were fitted using the Lifshitz-Kosevich formula with the fitting results shown in Fig. 8e. The analysis afforded a low cyclotron in-plane effective mass (m*) value of only 0.14 ± 0.02 m_0, consistent with the theoretical prediction and the results of angle-resolved photoemission spectroscopy measurements. Taking inspiration from the discovery of Bi_2O_2Se, Dai *et al.* proposed that 2D Sb_2Te_2X (X = S, Se) should offer outstanding dynamic and thermal stability [83], as well as remarkable isotropic electron mobility based on DFT and the Keldysh nonequilibrium Green's function formalism [84, 85]. The carrier mobility of Sb_2Te_2X at 300 K was also investigated based on the deformation potential (DP) theory proposed by Bardeen and Shockley. Carrier migration for both samples occurred along with the armchair and zigzag directions, with the mobilities > 1000 cm^2 V^{-1} S^{-1} being superior to 2D MoS_2 (< 400 cm^2 V^{-1} S^{-1}) [76]. Such high mobilities are anticipated to greatly enhance the amount of photo-generated carriers available to participate in catalytic reactions, thereby delivering enhanced photocatalytic performance.

FIGURE 11

a) Schematic showing photocatalytic CO_2 reduction to CO. b) DFT-calculated adsorption energies of CO_2 and H_2O molecules on defect-rich ZnAl-LDH and bulk ZnAl-LDH. c) Charge-density distribution for the valence band maximum of the defect-rich ZnAl-LDH [40]. Copyright 2015, Wiley-VCH. d) The reaction mechanism of OER and e) Standard free energy diagrams for OER on MCr-LDHs (M = Cu, Zn and Ni) [73]. Copyright 2017, American Chemical Society. f) Photocatalytic N_2 fixation process on the surface of ultrathin TiO_2 nanosheets. g) N≡N distance of N_2 on TiO_2-Pure, TiO_2-Vo, TiO_2-Vo-Strain, along with corresponding values for N_2H_2, and N_2H_4. h) Calculated free energy diagram for N_2 fixation over the (001) surface of TiO_2-Pure, TiO_2-Vo and TiO_2-Vo-Strain [103]. Copyright 2019, Wiley-VCH.

2.5 Reaction energy

Different crystal facets expose different arrangements of atoms. Lower energy surfaces are more stable [47, 86], whereas high energy surfaces that maximize the exposure of atoms with low coordination numbers (relative to bulk) are generally more reactive in catalysis. Accordingly, the synthesis of catalysts preferentially exposing high

energy crystal facets represents an effective approach for maximizing performance. In pursuit of this goal, the effect of adsorbing 12 non-metallic atoms (X = H, B, C, N, O, F, Si, P, S, Cl, Br, or I) on the surface energies of anatase (001) and (101) surfaces were theoretically investigated [87]. It was found that the adsorption of F lowered the surface energy of specific facets, resulting in the preferential exposure of {001} facets. In most computational studies, the formation energy is also calculated to determine the most stable structure(s) for a reference for modification strategies [88]. In 2016, Zhang's group reported the precise regulation of internal electric field (IEF) in bulk Bi_3O_4Cl, achieving a 126 times increase of IEF and a bulk-charge separation efficiency of 80% [89]. Crystal models of X-doped Bi_3O_4Cl (X= P, S, N, B, F, Br, C) were constructed, with the calculations revealing that the X atoms substituted into Cl in the [Cl] layers rather Bi or O in the $[Bi_3O_4]$ layers. Charge density contour plots showed that amongst the elements tested, C doping caused the largest nonuniform distribution of charge between the $[Bi_3O_4]$ and [Cl] layers. Moreover, the electrostatic potential difference (ΔE) between the $[Bi_3O_4]$ and [Cl] layers was investigated. The calculations determined that carbon-doped Bi_3O_4Cl possessed the highest ΔE value (7.36 eV), indicating carbon doping was the most effective strategy for enhancing the IEF in Bi_3O_4Cl. Inspired by the theoretical simulation results, carbon-doped Bi_3O_4Cl was synthesized. To probe how the large IEF enhanced photogenerated electron and hole separation, femtosecond-resolved transient absorption spectroscopy (TAS) was applied. The analysis revealed that the build-up of the excited-state absorption signal required only 1 ps for carbon-doped Bi_3O_4Cl, whereas 20 ps was required for bulk Bi_3O_4Cl. The 4000 ps charge decay for carbon-doped Bi_3O_4Cl provided solid experimental evidence that the large IEF was effective in restricting charge recombination during their migration from the bulk to the surface [90]. Ultra-fast electron hopping due to the presence of the large IEF was suggested by DFT calculations and experiment [91]. For all catalytic reactions, physical adsorption, bonding and activation of reactants are important. For reactant adsorption, the adsorption energy is widely used to determine which catalyst is most suitable to drive a particular reaction [42, 92, 93]. For photocatalytic CO_2 reduction (Fig. 11a-b), ZnAl-LDH containing Zn^+-Vo sites exhibited a much higher adsorption energy for CO_2

(2.118 eV) relative defect-free ZnAl-LDH (0.537 eV). The adsorption energy of H_2O on the same surfaces followed the same trend (2.169 eV versus 0.980 eV) [40]. The data reveals that CO_2 and H_2O bind more strongly on LDH surfaces containing Vo. Fig. 11c shows that the charge density of the defective LDH mainly concentrates at the Zn atoms (Zn^+ sites neighboring Vo), which are identified as the active sites for CO_2 photoreduction in the presence of water vapor. Following chemical or physical adsorption, the adsorbate-adsorbent bond strength and activation energy barriers for desorption versus reaction determine the photocatalytic reaction path. For the photocatalytic hydrogen evolution reaction (HER) [94, 95], the free energy of the adsorbed state is calculated as $\Delta G_{H*} = \Delta E_H + \Delta E_{ZPE} - T\Delta S_H$, where ΔE_H is the hydrogen chemisorption energy and ΔE_{ZPE} is the difference in zero-point energy between the adsorbed and the gas phase. The chemical adsorption energy of H* on Pt (111) is much smaller than that values calculated for other metals, suggesting Pt possesses superior HER activity from a thermodynamic viewpoint. Two mechanisms have been proposed for the photocatalytic oxygen evolution reaction (OER) [96-99]. The overpotential (η) of the two mechanisms were calculated using similar methods (Fig. 11d). Wei and co-worker investigated the photocatalytic OER performance of twelve different kinds of LDHs. Ten of the LDHs were active for photocatalytic OER [73]. MgCr-LDH exhibited no OER activity, whilst NiCr-LDH, CuCr-LDH and NiCr-LDH possessed very good OER activity, as was predicted by theoretical studies (Fig. 11e). Recently, solar-driven ammonia photosynthesis has received a lot of attention, potentially offering a low energy input technology for making NH_3 from N_2 and H_2O under ambient conditions [52, 100-102]. Developing efficient photocatalytic materials for nitrogen fixation is highly desirable. Zhao *et al.* synthesized TiO_2 nanosheets with tunable concentrations of oxygen vacancies *via* a facile copper-doping strategy (Fig. 11f) [103]. Cu-doping introduced abundant Vo and strain into the TiO_2 nanosheets, thereby enhancing nitrogen adsorption and weakening N≡N bond which increased in length from 1.155Å to 1.163Å on adsorption (Fig. 11g). Further, the introduction of Vo and strain lowered the energy barrier of the rate-limiting step in ammonia synthesis, lowering the Gibbs free energy for the formation of N≡NH* from 2.115 eV to 0.223 eV (Fig. 11h). DFT calculations

studying reactant adsorption and reaction energies are therefore vital for rationalizing the performance of different catalysts, whilst also allowing the discovery of new reaction pathways.
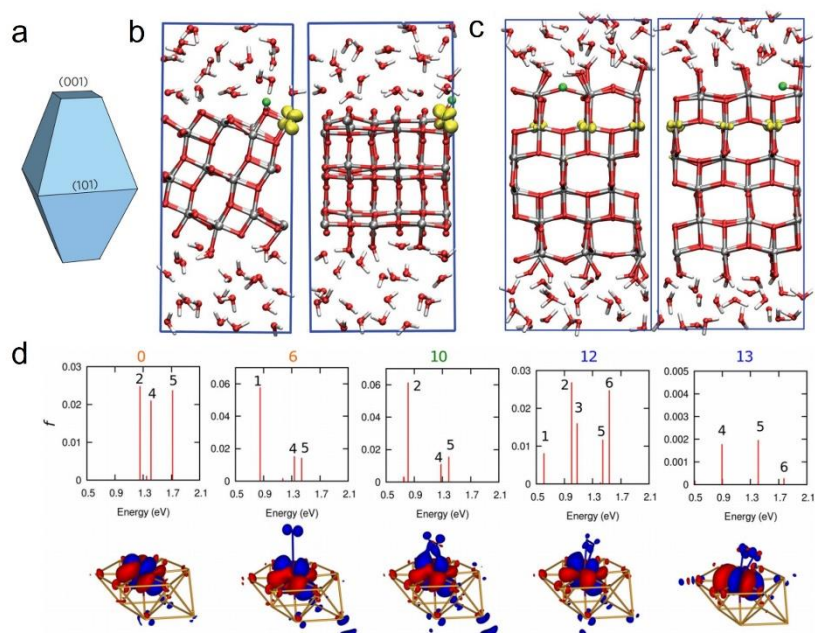
FIGURE 12

a) Wulff shape of an anatase crystal exposing of (101) and (001) surfaces. b-c) First-principles molecular dynamics simulations of Hydroxylated a-101 and a-001 slabs immersed in water, viewed from two different perspectives [104]. Copyright 2016, Nature Publishing Group. d) Oscillator strengths and electron density differences [105]. Copyright 2017, American Association for the Advancement of Science.

3. Conclusions and Perspectives

Herein, we have reviewed recent advancements in the design/development of 2D photocatalysts for different applications focusing on 5 key aspects: crystal structure, electronic structure, bandgap manipulation, charge carrier mobilities and reaction energies. The construction of accurate crystal structure models provides a basis for theoretical calculations, necessitating the determination of the unit cell parameters with high precision from experimental data. Since photocatalytic reactions occur on the

catalyst surface, the electronic structure of catalyst and exposed surface facets can greatly impact photocatalytic activity, which is especially relevant for 2D photocatalysts whose properties (e.g. band gap and band edge positions) oftern differ from their bulk counterparts. Minimizing electron-hole pair recombination and promoting electron transfer efficiency, both of which can generally be realized in defect-rich 2D systems, are further steps towards improved photocatalytic performance. The design/development of efficient photocatalysts therefore needs to be considered from multiple viewpoints, followed by rigorous optimization of photocatalyst testing conditions.

Whilst 2D photocatalyst research has developed rapidly in recent years, leveraging both theoretical and experimental breakthroughs, step-change improvements in photocatalyst performance require a number of key bottlenecks to be overcome. Main challenges that need to be addressed include:

i) Most photocatalytic reactions involve solid-liquid or gas-solid reaction systems, thus it is necessary to consider how the various molecules in the photocatalyst system might adsorb on the photocatalyst and influence the calculation of reaction energies and barrier heights. Calculation models need thus to be able to realistically simulate the experimental testing conditions in order to be relevant and useful.

ii) The photo-excitation of a semiconductor photocatalyst (1D, 2D or 3D) creates photo-generated electrons and holes, leaving the photocatalyst in an excited state. Understanding the dynamics of excited electrons is therefore important to understanding photocatalytic processes. Selcuk and Selloni established from first-principles simulations that the behavior of excited electrons on anatase surfaces depended strongly on the nature of the exposed facet, the environment and the character of the electron donor during the photocatalytic reaction (Fig. 12a-c). Time-dependent density functional theory (TD-DFT) calculations are invaluable for probing excited-state chemistry during photocatalysis [104]. For example, using embedded multireference correlated wave function calculations, Mo doping into Au surfaces was found to lower the energy barrier for N_2 activation, from 3.5 eV/N_2 for a pure Au surface to 0.44 eV/N_2 for a Mo-doped Au surface, thus overcoming the key bottleneck in NH_3

production (Fig. 12d) [105]. The Au acted as the light-capturing agent, transferring energy onto the Mo active site, thereby exploiting excited-state channels to overcome the limitation of the catalyst in the ground state.

iii) The surfaces of photocatalysts are dynamic, frequently undergoing change as the reaction proceeds. To capture information on the surface of the catalyst as a function of reaction time, time-resolved spectroscopy and femtosecond transient absorption spectroscopy are invaluable techniques. Theoretical simulations would therefore require dynamic rather than static crystal models. Thus, novel simulation methods or using dynamics simulation algorithms therefore need to overcome this current limitation.

Over the next decade, the combination of theory and experiment will increasingly be applied in parallel, rather than consecutively, for the deeper understanding of photocatalytic reactions. Coupled with advances in ultrafast characterization techniques and new dynamic simulation algorithm, step-change improvements in photocatalyst performance should be possible, with 2D photocatalysts expected to play a pivotal role on the pathway to practical photocatalyst systems for industry.

References

[1] H. Tong et al., Adv. Mater. 24 (2012) 229-251.

[2] T. Hisatomi et al., Chem. Soc. Rev. 43 (2014) 7520-7535.

[3] J. Kou et al., Chem. Rev. 117 (2017) 1445-1514.

[4] T.L. Thompson, J.T. Yates, Chem. Rev. 106 (2006) 4428-4453.

[5] A. Fujishima et al., J. Photoch. Photobio C 1 (2000) 1-21.

[6] A. Fujishima, K. Honda, Nature 238 (1972) 37-38.

[7] M.G. Walter et al., Chem. Rev. 110 (2010) 6446-6473.

[8] D.M. Schultz, T.P. Yoon, Science 343 (2014) 1239176.

[9] J.C. Colmenares, R. Luque, Chem. Soc. Rev. 43 (2014) 765-778.

[10] X. Chia, M. Pumera, Nat. Catal. 1 (2018) 909-921.

[11] C. Tan, H. Zhang, Nat. Commun. 6 (2015) 7873.

[12] H. Zhang, ACS nano 9 (2015) 9451-9469.

[13] X. Chia et al., Chem. Rev. 115 (2015) 11941-11966.

[14] L. Sheng et al., Mater. Today Energy 3 (2017) 32-39.

[15] X. Zhang et al., J. Phys. Chem. C 112 (2008) 747-753.

[16] Q. Wang, D. O'Hare, Chem. Rev. 112 (2012) 4124-4155.

[17] K. Watanabe et al., Nat. Mater. 3 (2004) 404-409.

[18] Y. Wang et al., Angew. Chem. Int. Ed. 51 (2012) 68-89.

[19] B. Anasori et al., Nat. Rev. Mater. 2 (2017) 16098.

[20] L. Li et al., Nat. Nanotechnol. 9 (2014) 372-377.

[21] Y. Li et al., Mater. Today Chem. 11 (2019) 197-216.

[22] W. Yang et al., Nano Today 11 (2016) 793-816.

[23] C.F. Fu et al., Adv. Mater. 30 (2018) 1802106.

[24] J. Li et al., Nat. Commun. 7 (2016) 11480.

[25] J. Di et al., Adv. Mater. 31. (2019) 1807576.

[26] B. Choudhury, M. Dey, A. Choudhury, Int. Nano Lett. 3 (2013) 25.

[27] X. Wang et al., Nat. Mater. 8 (2009) 76-80.

[28] K. Maeda et al., J. Phys. Chem. C 113 (2009) 4940-4947.

[29] J. Liu et al., Science 347 (2015) 970-974.

[30] Y. Zheng et al., Angew. Chem. Int. Ed. 53 (2014) 11926-11930.

[31] F. Su et al., J. Am. Chem. Soc. 132 (2010) 16299-16301.

[32] T.M. Alam, Mater. Chem. Phys. 85 (2004) 310-315.

[33] B. Jürgens et al., J. Am. Chem. Soc. 125 (2003) 10288-10300.

[34] V.W.-h. Lau et al., Nat. Commun. 7 (2016) 12165.

[35] H. Yu et al., Adv. Mater. 29 (2017) 1605148.

[36] Y. Zhao et al., Chem. Mater. 14 (2002) 4286-4291.

[37] J. He et al., Layered double hydroxides, Springer, 2006, pp. 89-119.

[38] S. He et al., Chem. Commun. 49 (2013) 5912-5920.

[39] X. Duan, D.G. Evans, Layered double hydroxides, Springer Science & Business Media, 2006.

[40] Y. Zhao et al., Adv. Mater. 27 (2015) 7824-7831.

[41] W. Wang et al., Adv. Mater. 31 (2019) 1808276.

[42] C. Mao et al., Appl. Catal., B 228 (2018) 87-96.

[43] H. Li et al., Nanoscale 6 (2014) 14168-14173.

[44] K. Zhang et al., Cryst. Growth Des. 12 (2012) 793-803.

[45] B. Yang et al., Sci. China Chem. 61 (2018) 1572-1580.

[46] A. Selloni, Nat. Mater. 7 (2008) 613-615.

[47] Y. Bi et al., J. Am. Chem. Soc. 133 (2011) 6490-6492.

[48] S. Chen et al., Nat. Commun. 10 (2019) 788.

[49] H. Wang et al., J. Am. Chem. Soc. 140 (2018) 1760-1766.

[50] N. Zhang et al., J. Am. Chem. Soc. 138 (2016) 8928-8935.

[51] J. Wu et al., Angew. Chem. Int. Ed. 130 (2018) 8855-8859.

[52] H. Li et al., J. Am. Chem. Soc. 137 (2015) 6393-6399.

[53] C. Xiao et al., J. Am. Chem. Soc. 134 (2012) 18460-18466.

[54] X. Liu et al., J. Am. Chem. Soc. 131 (2009) 3140-3141.

[55] L. Liang et al., J. Am. Chem. Soc. 137 (2015) 3102-3108.

[56] M. Guan et al., J. Am. Chem. Soc. 135 (2013) 10411-10417.

[57] G. Liu et al., Chem. Soc. Rev. 47 (2018) 6410-6444.

[58] J. Di et al., Adv. Mater. 30 (2018) 1704548.

[59] Y. Gai et al., Phys. Rev. Lett. 102 (2009) 036402.

[60] W. Zhu et al., Phys. Rev. Lett. 103 (2009) 226401.

[61] W.-J. Yin et al., Phys. Rev. Lett. 106 (2011) 066801.

[62] A.N. Rudenko, M.I. Katsnelson, Phys. Rev. B 89 (2014) 201408.

[63] A. Splendiani et al., Nano Lett. 10 (2010) 1271-1275.

[64] K.F. Mak et al., Phys. Rev. Lett. 105 (2010) 136805.

[65] K. Akatsuka et al., J. Phys. Chem. C 116 (2012) 12426-12433.

[66] C. Zhou et al., Chem. Commun. 50 (2014) 9554-9556.

[67] C. Zhou et al., ChemPlusChem 82 (2017) 181-185.

[68] C. Zhou et al., Chem. Commun. 52 (2016) 8239-8242.

[69] N. Sakai et al., J. Am. Chem. Soc. 126 (2004) 5851-5858.

[70] S.L. Wang et al., J. Am. Chem. Soc. 139 (2017) 15414-15419.

[71] J. Li et al., Acc. Chem. Res. 50 (2016) 112-121.

[72] S.-M. Xu et al., J. Phys. Chem. C 119 (2015) 18823-18834.

[73] S.-M. Xu et al., J. Phys. Chem. C 121 (2017) 2683-2695.

[74] T. Li et al., Phys. Chem. Chem. Phys. 21 (2019) 868-875.

[75] Z.-Y. Zhao, W.-W. Dai, Inorg. Chem. 53 (2014) 13001-13011.

[76] S.-L. Li et al., Chem. Soc. Rev. 45 (2016) 118-151.

[77] L. Li et al., Nat. Nanotechnol. 12 (2017) 21-25.

[78] X. Zhang et al., Adv. Sci. 3 (2016) 1600062.

[79] A. Rudenko et al., Phys. Rev. Lett. 116 (2016) 246401.

[80] J. Wu et al., Nat. Nanotechnol. 12 (2017) 530-534.

[81] J. Wu et al., Nano Lett. 17 (2017) 3021-3026.

[82] M. Wu, X.C. Zeng, Nano Lett. 17 (2017) 6309-6314.

[83] Y. Liang et al., Phys. Chem. Chem. Phys. 21 (2019) 14904-14910.

[84] J. Chen et al., Phys. Rev. B 85 (2012) 155441.

[85] D. Waldron et al., Phys. Rev. Lett. 96 (2006) 166804.

[86] G. Liu et al., Chem. Rev. 114 (2014) 9559-9612.

[87] H.G. Yang et al., Nature 453 (2008) 638-641.

[88] L. Li et al., Nanoscale 6 (2014) 24-42.

[89] J. Li et al., Adv. Mater. 28 (2016) 4059-4064.

[90] R. Li et al., Adv. Mater. 26 (2014) 4783-4788.

[91] F. Lei et al., Angew. Chem. Int. Ed. 54 (2015) 9266-9270.

[92] M. Calandra, Phys. Rev. B 88 (2013) 245428.

[93] Y. Zhao et al., Adv. Energy Mater. 7 (2017) 1700005.

[94] J.K. Nørskov et al., J. Electrochem. Soc. 152 (2005) J23-J26.

[95] D. Vanderbilt, Phys. Rev. B 41 (1990) 7892.

[96] A. Valdes et al., J. Phys. Chem. C 112 (2008) 9872-9879.

[97] M. Bajdich et al., J. Am. Chem. Soc. 135 (2013) 13521-13530.

[98] M. García-Mota et al., J. Phys. Chem. C 116 (2012) 21077-21082.

[99] M. Lyons et al., J. Electrochem. Soc. 159 (2012) H932-H944.

[100] Y. Zhao et al., Adv. Mater. 29 (2017) 1703828.

[101] X. Chen et al., Mater. Horiz. 5 (2018) 9-27.

[102] C. Guo et al., Energy Environ. Sci. 11 (2018) 45-56.

[103] Y. Zhao et al., Adv. Mater. 31 (2019) 1806482.

[104] S. Selcuk, A. Selloni, Nat. Mater. 15 (2016) 1107-1112.

[105] J.M.P. Martirez, E.A. Carter, Sci. Adv. 3 (2017) eaao4710.